



INSTITUT DE FRANCE  
Académie des sciences

# *Comptes Rendus*

---

## *Chimie*


Fatma-Zohra Maiouf, Abdenour Boumechhour, Siham Benadji,  
Leila Dermeche, Tassadit Mazari, Christine Lancelot and Chérifa  
Rabia

**Preparation, characterization of mixed-valence antimony-tin  
phosphomolybdc polyoxometalates and application in the  
cyclohexanone oxidation in the presence of hydrogen peroxide**

Volume 25 (2022), p. 253-266

Published online: 6 September 2022

<https://doi.org/10.5802/crchim.195>

 This article is licensed under the  
CREATIVE COMMONS ATTRIBUTION 4.0 INTERNATIONAL LICENSE.  
<http://creativecommons.org/licenses/by/4.0/>



*Les Comptes Rendus. Chimie* sont membres du  
Centre Mersenne pour l'édition scientifique ouverte  
[www.centre-mersenne.org](http://www.centre-mersenne.org)  
e-ISSN : 1878-1543



Full paper / Article

# Preparation, characterization of mixed-valence antimony-tin phosphomolybdic polyoxometalates and application in the cyclohexanone oxidation in the presence of hydrogen peroxide

Fatma-Zohra Maiouf<sup>✉</sup>\*, <sup>a</sup>, Abdenour Boumechhour<sup>✉</sup> <sup>a, b</sup>, Siham Benadji<sup>a</sup>,  
Leila Dermeche<sup>c</sup>, Tassadit Mazari<sup>c</sup>, Christine Lancelot<sup>d</sup> and Chérifa Rabia<sup>a</sup>

<sup>a</sup> Laboratoire de Chimie du Gaz Naturel, Faculté de Chimie, USTHB, BP32, El-Alia, 16111 Bab-Ezzouar, Alger, Algeria

<sup>b</sup> Centre de Recherche en Analyses Physico-chimiques (CRAPC), BP 384 RP 42004 Bou-Ismaïl, Tipaza, Algeria

<sup>c</sup> Laboratoire de Chimie Appliquée et de Génie Chimique, Université Mouloud-Mammeri (UMMTO), BP 17 RP 15000 Tizi-Ouzou, Algeria

<sup>d</sup> Unité de catalyse et chimie du solide, UMR 8181 Université de Lille Cité Scientifique, Bâtiment C359650 Villeneuve d'Ascq Cedex, France

*E-mails:* fmaiouf@usthb.dz, fatmazohramaiouf@gmail.com (F.-Z. Maiouf), b.abdenour@gmail.com (A. Boumechhour), s\_benadji@yahoo.fr (S. Benadji), der\_lila@yahoo.fr (L. Dermeche), tassadit.mazari@ummto.dz (T. Mazari), christine.lancelot@univ-lille.fr (C. Lancelot), c\_rabia@yahoo.fr (C. Rabia)

**Abstract.** In this work, a series of polyoxometalates (POMs), as soluble salts of formula  $\text{Sn}_{1.5}\text{PMo}_{12}\text{O}_{40}$ ,  $\text{SbPMo}_{12}\text{O}_{40}$  and  $\text{H}_{3-x}\text{Sn}_{x1}\text{Sb}_{x2}\text{PMo}_{12}\text{O}_{40}$  ( $x = 2x_1 + 3x_2$  and  $x_1, x_2 = 0-0.75$ ) were synthesized using the cationic exchange method under stoichiometric conditions. They were characterized and tested in the oxidation of cyclohexanone using hydrogen peroxide in the absence of organic solvent, co-catalyst phase transfer compounds or surfactants. UV-Visible and X-ray photoelectron spectroscopic analyses showed a partially reduced state of POM with coexistence of the couples Mo(VI)/Mo(V), Sb(V)/Sb(III) and Sn(IV)/Sn(II), without affecting their structure, results confirmed by FT-IR and Raman spectroscopies. The reversible cyclic voltammetry analysis evidenced the valence change of the Mo species, Mo(VI)/Mo(V). The POMs are found to be active in the cyclohexanone oxidation reaction and among them the most efficient is  $\text{H}_{0.75}\text{Sb}_{0.75}\text{PMo}_{12}\text{O}_{40}$  with 49% of adipic acid yield.

**Keywords.** Polyoxometalates, Mixed-valence salts, Cyclohexanone, Oxidation, Adipic acid.

*Manuscript received 6 November 2021, revised 18 March 2022 and 2 June 2022, accepted 2 June 2022.*

\* Corresponding author.

## 1. Introduction

The oxidation of organic compounds into oxygenated compounds, used as precursors or intermediates, is of great importance in organic syntheses [1–3]. In the field of green chemistry, several works focus their research on efficient catalytic systems exploiting clean oxidants such as molecular oxygen, hydrogen peroxide and non-corrosive and non-polluting catalytic materials [4–8]. In this context, Keggin-type polyoxometalates (POMs), especially those based on the phosphomolybdic ion ( $\text{PMo}_{12}\text{O}_{40}^{3-}$ ) can meet these requirements. They are widely used as homogeneous and heterogeneous catalysts in acid and/or oxidative reactions due to their multifunctional properties, combined with their chemical composition that can be modulated according to the needs of the desired reaction [9–11]. POMs with higher oxidation state ( $\text{Mo}^{\text{VI}}$ ) are also recognized as electron reservoirs due to the vacant d-orbitals of the transition metal [12–14]. Furthermore, it has been shown that in the presence of hydrogen peroxide, POMs form peroxide species whose catalytic action is more effective than that of POMs [15–18].

The POM synthesis has been elaborated to adapt the process to the objectives. In order to increase the oxidizing power of POMs, several studies have proposed the introduction of transition metals (Co, Ni, Fe, Mn, ...) and non-metallic elements (Sb, Sn, Bi, ...) as a counter-ion using the precipitation method from the parent heteropolyacid (HPA) in the presence of ammonium chloride or cesium chloride [19–25]. The introduction of antimony or tin in the POM-framework has already been the subject of several studies [22,26–31]. The authors have prepared mixed-valence antimony POMs such as  $[\text{Sb}_4^{\text{V}}\text{Sb}_2^{\text{III}}\text{Mo}_{18}\text{O}_{73}(\text{H}_2\text{O})_2]^{12-}$  and  $\{\text{M}(\text{H}_2\text{O})_2[\text{Sb}_4^{\text{V}}\text{Sb}_2^{\text{III}}\text{Mo}_{18}\text{O}_{73}(\text{H}_2\text{O})_2]_2\}^{22-}$  (M:  $\text{Mn}^{\text{II}}$ ,  $\text{Fe}^{\text{II}}$ ,  $\text{Cu}^{\text{II}}$  or  $\text{Co}^{\text{II}}$ ),  $\text{Na}_{10}\{[\text{Sb}^{\text{V}}(\text{OH})_3]_2\{\text{V}^{\text{IV}} - \text{O}(\text{H}_2\text{O})\}_2\{\text{Sb}^{\text{III}}\text{W}_9\text{O}_{33}\}_2\}32\text{H}_2\text{O}$  and  $[\text{Sb}^{\text{V}}\text{Sb}_4^{\text{III}}\text{Mo}_{18}\text{O}_{66}]^{7-}$  using both  $\text{SbCl}_3$  and  $\text{Sb}_2\text{O}_5$ . Keggin-type POMs such as  $(\text{NH}_4)_x\text{A}_y\text{PMo}_{12}\text{O}_{40}$  and  $\text{Cs}_x\text{A}_y\text{PMo}_{12}\text{O}_{40}$  ( $\text{A}^{n+} = \text{Sb}^{3+}$ ,  $\text{Bi}^{3+}$  or  $\text{Sn}^{2+}$ ) were also prepared. In the case of  $\text{Sn}^{\text{II}}$  based POMs, the  $\text{Sn}^{\text{IV}}$  state is formed in situ, a presence that is demonstrated by XPS or UV-Visible (UV-Vis).

In this work, phosphomolybdic POMs were prepared by introducing tin and/or antimony

as more electronegative element than molybdenum, in the cationic position, in order to create more active sites with the formation of redox couples such as  $\text{Mo}(\text{VI})/\text{Mo}(\text{V})$ ,  $\text{Sb}(\text{V})/\text{Sb}(\text{III})$  and  $\text{Sn}(\text{IV})/\text{Sn}(\text{II})$  in situ. Thus, a series of POMs as *soluble salts* of formula  $\text{Sn}_{1.5}\text{PMo}_{12}\text{O}_{40}$ ,  $\text{SbPMo}_{12}\text{O}_{40}$  and  $\text{H}_{3-x}\text{Sn}_{x_1}\text{Sb}_{x_2}\text{PMo}_{12}\text{O}_{40}$  ( $x = 2x_1 + 3x_2$  and  $x_1, x_2 = 0-0.75$ ) was prepared using the cationic exchange method under stoichiometric conditions. This method permits to fix the number of Sn and Sb atoms from 0.25 to 1.5, in contrast to that of the precipitation where the number of these atoms is arbitrary; even if initially fixed [19,23,32]. In this case, the number of these atoms must be determined by ICP analysis. The prepared materials were characterized by several physicochemical techniques such as Raman, Fourier Transform-Infrared (FT-IR), solid UV-Vis and X-ray Photoelectron (XPS) spectroscopies and X-ray diffraction (XRD), thermogravimetric analysis (TG-DTA) and electrochemical analysis (cyclic voltammetry) and tested in the cyclohexanone oxidation in the presence of hydrogen peroxide at 90 °C, without the addition of organic solvent, co-catalyst, phase transfer compounds or surfactants, which are harmful reagents, as observed in several studies [33]. Among the products of the cyclohexanone oxidation, adipic acid (AA) is the most important because of its use as a precursor in the production of Nylon-6,6, polyvinyl butyral (PVB), and as additives for food, cosmetics, gelatins, lubricants, fertilizers, adhesives, insecticides, paper and waxes [34–36]. In this study, only the AA formation was taken into account. It can be easily separated from the other products of the oxidation reaction by cold crystallization.

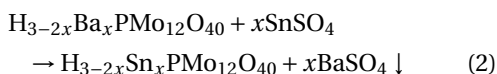
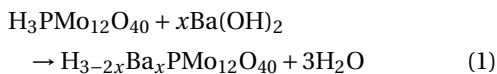
## 2. Experimental

### 2.1. Material synthesis

$\text{H}_3\text{PMo}_{12}\text{O}_{40}$  HPA was prepared according to the classical method described by Tsigdinos [37]. It is constituted of two steps, in the first one,  $\text{Na}_2\text{HPMo}_{12}\text{O}_{40}$  was synthesized by dissolving  $\text{Na}_2\text{MoO}_4$ , 2H<sub>2</sub>O (145.15 g) in 210 mL of distilled water, subsequently 3.4 mL of  $\text{H}_3\text{PO}_4$  (14.8 M) and 142 mL of  $\text{HClO}_4$  (11.7 M) were added to the solution. The mixture was left under stirring for 30 min. The yellow precipitate formed was then filtered and dried. In the second step, the recovered salt (125 g)

was dissolved in 150 mL of acidified water with 37.5 mL of HCl (2 M). The HPA was extracted with 130 ml of diethyl ether. The etherate-phase recovered was dissolved in half of its volume in water. Yellow translucent crystals were formed.

$\text{Sn}_{1.5}\text{PMo}_{12}\text{O}_{40}$ ,  $\text{SbPMo}_{12}\text{O}_{40}$  and  $\text{H}_{3-x}\text{Sn}_{x1}\text{Sb}_{x2}\text{PMo}_{12}\text{O}_{40}$  ( $x = 2x_1 + 3x_2$  and  $x_1, x_2 = 0-0.75$ ) *soluble salts* were synthesized using the cationic exchange method under stoichiometric conditions [19,23]. The method consists in a first step of adding progressively, in small quantities, solid  $\text{Ba}(\text{OH})_2$  to the HPA solution, maintaining  $\text{pH} < 2$  to avoid brutal decomposition of the Keggin anion (1). In the second step, the  $\text{Ba}^{2+}$  ions were precipitated as  $\text{BaSO}_4$  by adding metal sulfate ( $\text{SnSO}_4$  and/or  $\text{Sb}_2(\text{SO}_4)_3$ ) (2). After filtration, the soluble heteropolysalt was dried at  $50^\circ\text{C}$  under vacuum and recovered as a powder.



## 2.2. Characterization

Thermal analysis was performed from room temperature to  $600^\circ\text{C}$ , under  $\text{N}_2$  flow with a heating rate of  $5^\circ\text{C}/\text{min}$  using a TA Q600 apparatus.

IR spectroscopy ( $1800-400\text{ cm}^{-1}$ ) was performed using a Nicolet Is50 FT-IR spectrometer, including an attenuated total reflectance (ATR) module with a diamond crystal.

Raman spectra were obtained using an EXOLORA HORIBA spectrometer equipped with a detector operating at liquid nitrogen temperature under a double frequency Nd-YAG laser, with the excitation line at 532 nm. The samples were dispersed on a glass plate and the laser was focused on several grains under the microscope before the spectrum acquisition. Calibration was checked by using the Si line at 521 nm and/or the  $\text{MoO}_3$  line at 818 nm. The use of filters reduced the possibility of laser-induced changes in the solid state (applied power 0.04 mW).

UV-Vis spectra were performed with a Perkin Elmer UV/Vis spectrometer (Lambda 650S) equipped with an integrating sphere. The apparatus is constituted of a double beam and a double monochromator. The sources used are tungsten-halogen and deuterium. The solids are analyzed as finely ground pow-

der. The spectra of the solid samples were recorded between 200 and 900 nm with a step of 1 nm. For solids, the spectra collected in percent reflectance were processed by applying the Kubelka-Munk function to the raw data:  $F(R) = (1 - R)^2/2R$ .

XRD spectra were obtained using a Bruker D8 Advance A25 in Bragg-Brentano configuration (Cu  $K\alpha$  radiation,  $\lambda = 1.5418\text{ \AA}$ ), equipped with a 1D Lynxeye XE detector, in the range of  $2\theta = 5^\circ-70^\circ$ .

XPS measurements were carried out on a Kratos AXIS Ultra DLD spectrometer equipped with a monochromatic Al  $K\alpha$  X-ray source (10 mA, 12 kV), equipped with a hemispherical analyzer operating at a fixed pass energy of 20 eV. The pressure during analysis was lower than  $5 \times 10^{-9}$  mbar. Calibration was done by using the C 1s component of adventitious carbon at BE (binding energy) = 284.8 eV. Quantification and decomposition were carried out using Casa XPS software. A Shirley background was subtracted from the spectra for quantification. The analyzed area was of approximately  $700\text{ }\mu\text{m} \times 300\text{ }\mu\text{m}$ .

The Cyclic voltammograms were carried out at room temperature, on a PGZ 301 Potentiostat, in a conventional cell containing Hg/HgCl<sub>2</sub> electrode (SCE) and Pt-counter-electrode, the working electrode was prepared by dissolving 100 mg of catalyst in 200 ml of distilled water. The electrical current must be uniform; so the electrode was placed in front of the Pt electrode.

## 2.3. Catalytic reaction

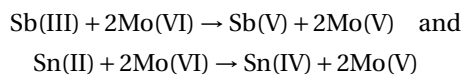
The cyclohexanone oxidation was performed according to the literature [38]. The mixture, constituted of the substrate (cyclohexanone) and the catalyst, was introduced into a 100 mL round-bottomed flask (1000 rpm) equipped with a reflux condenser and heated to  $90^\circ\text{C}$ . After a few minutes, the yellow reaction mixture turned blue, a typical color of reduced POM. 0.5 mL of hydrogen peroxide (30%) was then added to oxidize the reduced catalyst and restore the original yellow color. This operation is repeated after each color change. Once there is no further color change, indicating the end of the reaction, the mixture is stirred for up to 20 h to favor the AA formation. The reaction mixture is then cooled to  $4^\circ\text{C}$  overnight. The AA was recovered as white crystals and its purity was confirmed by recording its infrared spectrum and measuring its melting point ( $152^\circ\text{C}$ ).

### 3. Results and discussion

#### 3.1. Characterization results

##### 3.1.1. UV-Vis characterization

The UV-Vis spectra of solids of  $\text{H}_3\text{PMo}_{12}\text{O}_{40}$  and the different prepared salts (Figure 1) showed two absorption bands corresponding to ligand-metal charge transfers from oxygen to Mo(VI) [39,40]. The absorption band  $\text{O}_d \rightarrow \text{Mo}$  is located in the range of 223–227 nm and those corresponding to  $\text{O}_b/\text{O}_c \rightarrow \text{Mo}$  in the range of 319–334 nm. In the Keggin unit,  $\text{O}_a$  corresponds to O atoms shared in common between  $\text{PO}_4$  tetrahedron and a trimetallic group,  $\text{O}_b$  to O atoms connecting two trimetallic groups,  $\text{O}_c$  to O atoms connecting two  $\text{MoO}_6$  octahedra within a trimetallic group and  $\text{O}_d$  is a terminal oxygen, linked to a Mo atom [11]. The substitution of protons by Sn and/or Sb elements has led to the appearance of a wide charge transfer band around 700 nm, attributed to the d–d transition band of the Mo(V) [20,41]. The presence of this band suggests a partial reduction of Mo(VI) to Mo(V), highlighting an electron exchange between Sn(II) and Mo(VI) and Sb(III) and Mo(VI) as follows:



The intensity of the observed band at 700 nm, proportional to the amount of Mo(V) formed, is higher in the case of  $\text{Sn}_{1.5}\text{PMo}_{12}$ , suggesting that it has a higher reducing character than that of  $\text{SbPMo}_{12}$ .

Figure 1 also shows for  $\text{H}_{3-x}\text{Sn}_{x1}\text{Sb}_{x2}\text{PMo}_{12}\text{O}_{40}$  series, that the band intensity observed at 700 nm is sensitive to the stoichiometric coefficients of Sn and Sb atoms. When the Sn/Sb ratio is of 1 as in the case of  $\text{Sn}_{0.25}\text{Sb}_{0.25}$  and  $\text{Sn}_{0.5}\text{Sb}_{0.5}$ , the band intensity increases from 1.08 to 1.45 a.u., with the increase of the Sn and Sb atom number from 0.25 to 0.5 (Table 1). The intensity of the band is higher for a Sn/Sb ratio of 3 ( $\text{Sn}_{0.75}\text{Sb}_{0.25}$ ), than for a ratio of 1/3 ( $\text{Sn}_{0.25}\text{Sb}_{0.75}$ ), with 3.29 versus 2.52 a.u. These latter values are higher than those obtained in the case of  $\text{Sn}_{0.25}\text{Sb}_{0.25}$  and  $\text{Sn}_{0.5}\text{Sb}_{0.5}$  (1.08–1.45 a.u. for Sn/Sb = 1),  $\text{Sn}_{0.25}\text{Sb}_{0.5}$  (2.3 a.u. for Sn/Sb = 1/2) and  $\text{Sn}_0\text{Sb}_1$  (2.63 a.u. for Sn/Sb = 0/1). From these results, we can observe, that the partial reduction of POM can be adjusted as a function of the stoichiometric coefficients of Sn and Sb atoms. In the  $\text{H}_{3-x}\text{Sn}_{x1}\text{Sb}_{x2}\text{PMo}_{12}\text{O}_{40}$

series, the salt of formula  $\text{Sn}_{0.75}\text{Sb}_{0.25}$  appears to be the most reduced with more molybdenum atoms with an oxidation state V, therefore more Sn(IV) and Sb(V) ions.

##### 3.1.2. FT-IR and Raman spectroscopies

FT-IR spectra of  $\text{H}_3\text{PMo}_{12}\text{O}_{40}$  and Sn-, Sb-based salts (Figure 2) show the phosphorus–oxygen and molybdenum–oxygen characteristic vibration bands of the Keggin anion,  $[\text{PMo}_{12}\text{O}_{40}]^{3-}$ , in the low wavenumber region (1100–600  $\text{cm}^{-1}$ ). In accordance with the literature data [42], the asymmetric stretching  $\nu_{\text{as}}(\text{P}-\text{O}_a)$ , is observed at 1056–1054  $\text{cm}^{-1}$  and those of metal–oxygen,  $\nu_{\text{as}}(\text{Mo}-\text{O}_d)$ ,  $\nu_{\text{as}}(\text{Mo}-\text{O}_b-\text{Mo})$  and  $\nu_{\text{as}}(\text{Mo}-\text{O}_c-\text{Mo})$  at 952–949, 883–880 and 756–742  $\text{cm}^{-1}$ , respectively. Comparison of the frequency of the FT-IR vibration bands of  $\text{Sn}_x\text{Sb}_y\text{PMo}_{12}\text{O}_{40}$  salts, with those of the parent acid ( $\text{H}_3\text{PMo}_{12}\text{O}_{40}$ ) revealed no significant difference, except for  $\text{Sn}_{1.5}\text{PMo}_{12}\text{O}_{40}$  where a shift from 742 to 774  $\text{cm}^{-1}$  and a decrease in the intensity of the bands were observed, particularly that of  $\nu_{\text{as}}(\text{Mo}-\text{O}_c-\text{Mo})$ . These perturbations can be attributed to the presence of mixed-valence Sn(II) and Sn(IV) in the POM, that would lead to a deeper change in the symmetry of POM in contrast to the mixed Sn/Sb salt by formation of  $\text{Mo}^{\text{VI}}-\text{O}_c-\text{Mo}^{\text{V}}$  instead of  $\text{Mo}^{\text{VI}}-\text{O}_c-\text{Mo}^{\text{VI}}$ .

In conclusion, the Keggin anionic structure is well preserved despite the partially reduced state of POM, resulting from the introduction of Sb and/or Sn.

The Raman spectroscopy of the materials is shown in Figure 3. The phosphomolybdic acid,  $\text{H}_3\text{PMo}_{12}\text{O}_{40}$ , exhibits the characteristic Keggin anion vibrational bands in the wave number region of 1100–200  $\text{cm}^{-1}$ . According to the literature [20,43], the vibration bands observed at 998, 971, 908, 607 and 250  $\text{cm}^{-1}$  are attributed to  $\nu_s(\text{Mo}=\text{O}_d)$ ,  $\nu_{\text{as}}(\text{Mo}=\text{O}_d)$ ,  $\nu_{\text{as}}(\text{Mo}-\text{O}_b-\text{Mo})$ ,  $\nu_s(\text{Mo}-\text{O}_c-\text{Mo})$  and  $\nu_s(\text{Mo}-\text{O}_a)$ , respectively. An important decrease in the intensity of all vibration bands was observed on salt spectra, except in the case of  $\text{Sn}_{0.25}\text{Sb}_{0.25}$ , the less substituted. On the other hand, the shoulders attributed to  $\nu_{\text{as}}(\text{Mo}=\text{O}_d)$ ,  $\nu_{\text{as}}(\text{M}-\text{O}_b-\text{M})$  and  $\nu_s(\text{Mo}-\text{O}_c-\text{M})$  are not clearly visible on the spectra, particularly in the presence of tin. Furthermore, the frequency of  $\nu_s(\text{Mo}=\text{O}_d)$  has increased from 998 to 1009–1006  $\text{cm}^{-1}$  for all salts except for that of  $\text{Sn}_{0.25}\text{Sb}_{0.25}$ . These perturbations can be attributed to the partially reduced state of the heteropolyanion,

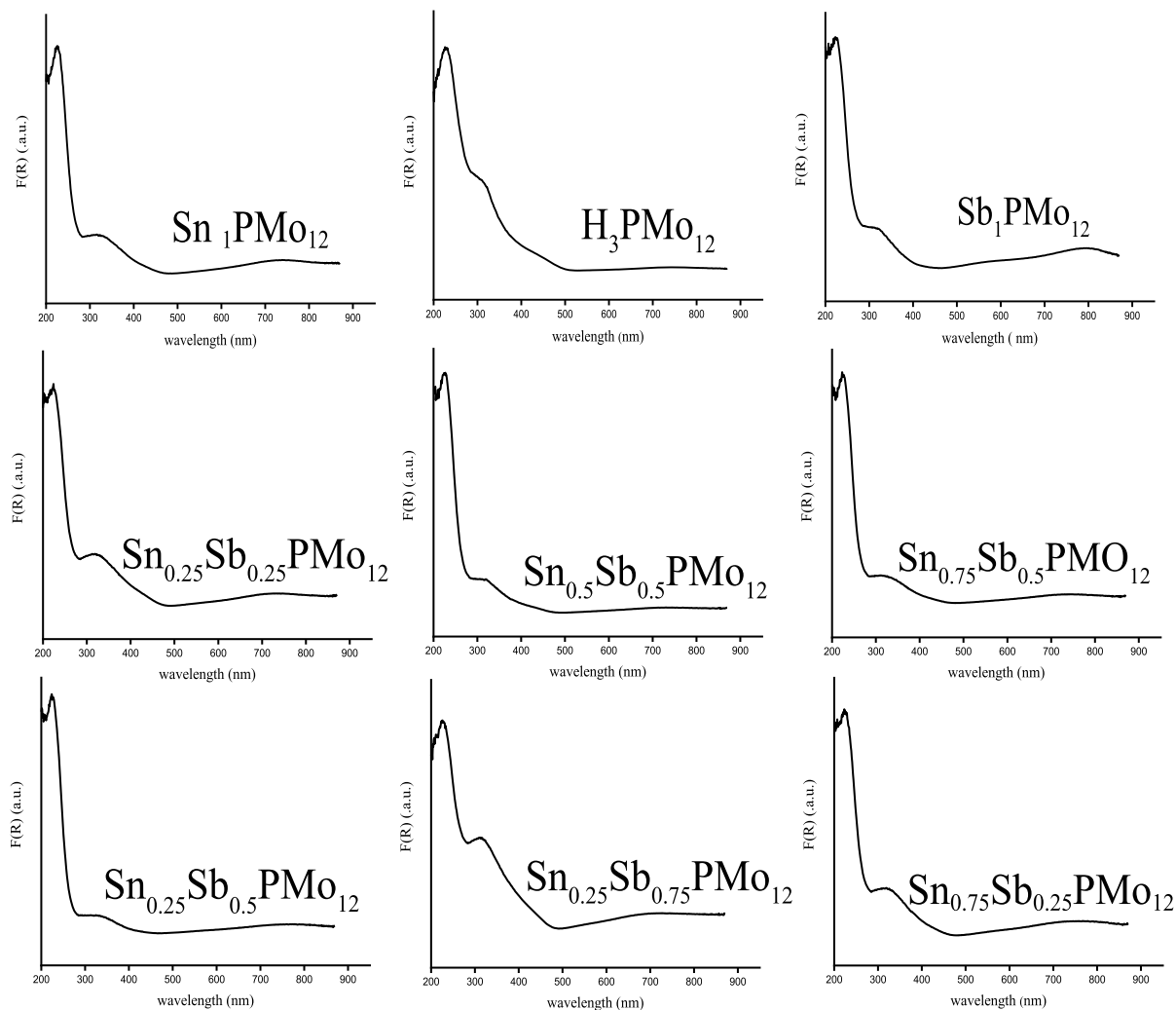


**Figure 1.** UV-Vis spectra of HPA,  $\text{Sn}_{1.5}\text{PMo}_{12}\text{O}_{40}$ ,  $\text{Sb}_1\text{PMo}_{12}\text{O}_{40}$  and  $\text{H}_{3-x}\text{Sn}_{x_1}\text{Sb}_{x_2}\text{PMo}_{12}\text{O}_{40}$  heteropolysalts ( $x_1, x_2 = 0-0.75$ ).

**Table 1.** d-d transition band intensities (a.u.) of Mo(V) in the heteropolysalts deduced from UV-Vis analysis

Catalyst	$\text{Sb}_1$	$\text{Sn}_{1.5}$	$\text{Sn}_{0.25}\text{Sb}_{0.25}$	$\text{Sn}_{0.25}\text{Sb}_{0.5}$	$\text{Sn}_{0.25}\text{Sb}_{0.75}$	$\text{Sn}_{0.5}\text{Sb}_{0.5}$	$\text{Sn}_{0.75}\text{Sb}_{0.25}$	$\text{Sn}_{0.75}\text{Sb}_{0.5}$
Band intensity (a.u.)	2.63	3.13	1.08	2.3	2.52	1.45	3.29	1.84

confirmed by the dark blue-green color of the salt as reported by Dermeche *et al.* [41]. Compared to FT-IR, Raman spectroscopy seems to be sensitive to the reduction of molybdenum (VI) induced by the introduction of antimony and tin. These results are in agreement with those observed in UV-Vis spec-

troscopy. It should be noted that the vibration band corresponding to  $\text{P-O}_a$  could not be observed by Raman spectroscopy.

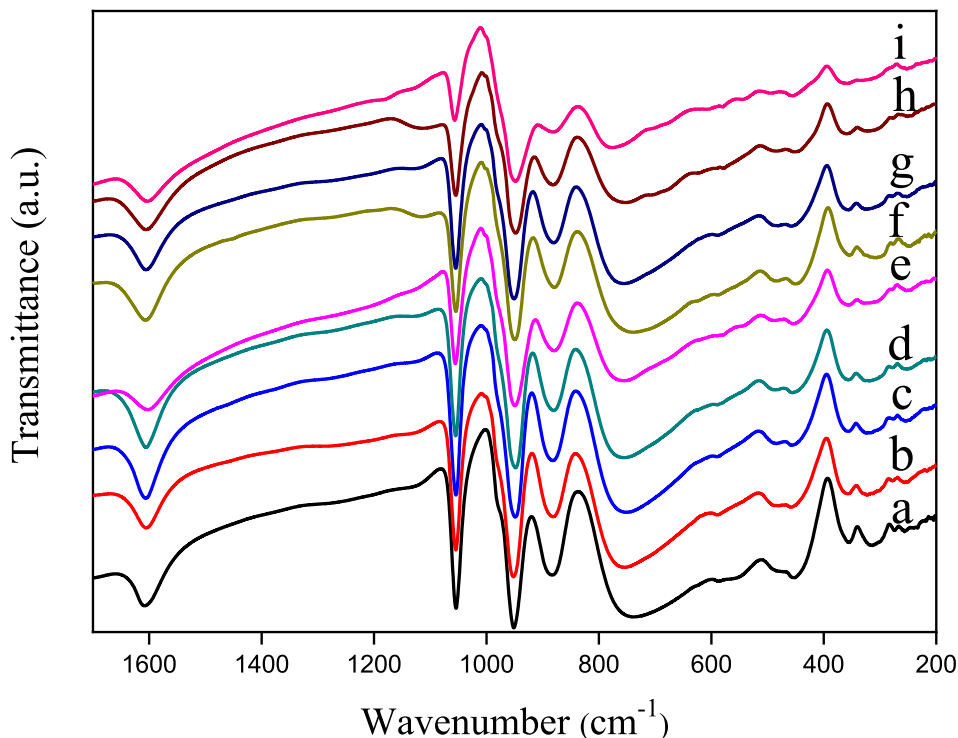


**Figure 2.** FT-IR spectra of  $\text{H}_3\text{PMo}_{12}\text{O}_{40}$  (a),  $\text{Sb}_{0.25}\text{Sn}_{0.25}\text{PMo}_{12}$  (b),  $\text{Sb}_{0.5}\text{Sn}_{0.5}\text{PMo}_{12}$  (c),  $\text{Sb}_{0.5}\text{Sn}_{0.75}\text{PMo}_{12}$  (d),  $\text{Sb}_{0.5}\text{Sn}_{0.25}\text{PMo}_{12}$  (e),  $\text{Sb}_{0.75}\text{Sn}_{0.25}\text{PMo}_{12}$  (f),  $\text{Sb}_{0.25}\text{Sn}_{0.75}\text{PMo}_{12}$  (g),  $\text{Sb}_1\text{PMo}_{12}$  (h) and  $\text{Sn}_{1.5}\text{PMo}_{12}$  (i).

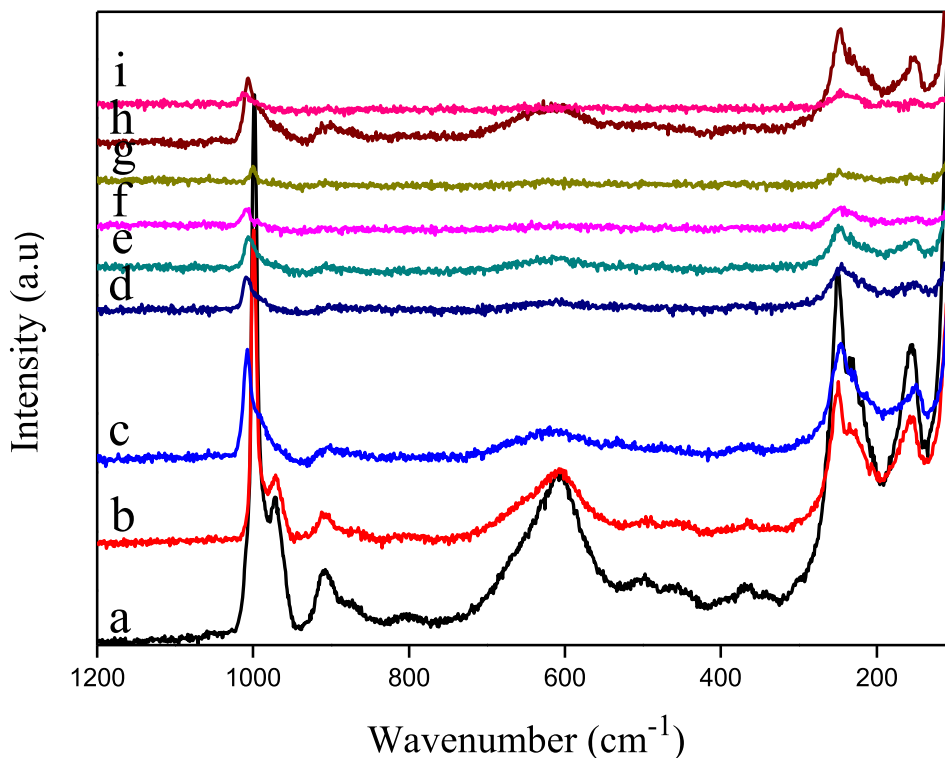
### 3.1.3. XRD characterization

Figure 4 shows that the XRD patterns of  $\text{Sn}_{1.5}\text{PMo}_{12}$ ,  $\text{SbPMo}_{12}$  and  $\text{H}_{3-2x}\text{Sn}_{x1}\text{Sb}_{x2}\text{PMo}_{12}\text{O}_{40}$  series are similar to that of the hydrated parent acid ( $\text{H}_3\text{PMo}_{12}\text{O}_{40}\cdot 13\text{H}_2\text{O}$ ) that crystallizes in a triclinic system (PDF-ICDD 075-1588). It is known that soluble salts corresponding to counter-ions of small ionic radius, classified in the group A category, crystallize in a system of low symmetry such as triclinic [44–47]. In the case of fully substituted salts ( $\text{Sn}_{1.5}\text{PMo}_{12}$ ,  $\text{SbPMo}_{12}$ ), the decrease in ray intensity demonstrates a loss of crystallinity, resulting in a distortion of the crystal lattice as reported in the literature [27,28,48]. It is also well known that the XRD and IR spectra reflect the secondary structure of the POM and the primary structure of the Keggin anion, respectively. In contrast to the Keggin structure, the secondary structure is of a crystalline system that is strongly dependent on the water molecule hydration number and both the nature and radius of the counter-ion. The loss of crystallinity is also attributed to the si-

multaneous presence of ions with different oxidation states such as  $\text{Sn(IV)/Sn(II)}$  and  $\text{Sb(V)/Sb(III)}$ , as observed in UV-Vis spectroscopy.

### 3.1.4. TG-DTA characterization

The TG-DTA curves of  $\text{H}_3\text{PMo}_{12}\text{O}_{40}$ ,  $\text{SbPMo}_{12}$  and  $\text{H}_{3-2x}\text{Sn}_{x1}\text{Sb}_{x2}\text{PMo}_{12}\text{O}_{40}$  series presented in Figure 5, are similar with two weight loss steps between 25 and 400 °C. The first (25–200 °C) is attributed to the desorption of the crystallization water molecules and the second (200–400 °C) to those of constitution and/or those accompanying the Sb and Sn counter-ions as  $[\text{M}(\text{H}_2\text{O})_x]^{n+}\text{M}^{n+}$ :  $\text{Sn}^{\text{II}}$ ,  $\text{Sn}^{\text{IV}}$ ,  $\text{Sb}^{\text{III}}$  and  $\text{Sb}^{\text{V}}$ . The higher the degree of oxidation, the more hydrated the ion [49]. This would explain the mass loss which extends from 200 to 400 °C. The DTA curves of all POMs show a strong exothermic peak around 440 °C, reflecting the crystallization of the different oxides originating from the decomposition of the POM ( $\text{P}_2\text{O}_5$ ,  $\text{MoO}_3$ ,  $\text{SnO/SnO}_2$ ,  $\text{Sb}_2\text{O}_3/\text{Sb}_2\text{O}_5$ ). Partial or total substitution of protons by antimony



**Figure 3.** Raman spectra of  $\text{H}_3\text{PMo}_{12}\text{O}_{40}$  (a),  $\text{Sb}_{0.25}\text{Sn}_{0.25}\text{PMo}_{12}$  (b),  $\text{Sb}_{0.5}\text{Sn}_{0.5}\text{PMo}_{12}$  (c),  $\text{Sb}_{0.5}\text{Sn}_{0.75}\text{PMo}_{12}$  (d),  $\text{Sb}_{0.5}\text{Sn}_{0.25}\text{PMo}_{12}$  (e),  $\text{Sb}_{0.75}\text{Sn}_{0.25}\text{PMo}_{12}$  (f),  $\text{Sb}_{0.25}\text{Sn}_{0.75}\text{PMo}_{12}$  (g),  $\text{Sb}_1\text{PMo}_{12}$  (h) and  $\text{Sn}_{1.5}\text{PMo}_{12}$  (i).

and/or tin ions does not appear to affect the thermal stability of POM.

### 3.1.5. XPS characterization

Table 2 presents the binding energies of elements, determined from XPS analysis. For  $\text{H}_3\text{PMo}_{12}\text{O}_{40}$ , taken as reference, the binding energies determined are 531.2 eV for oxygen (O 1s), 134.2 eV for phosphorus (P 2p) in its oxidation state V and 233.2 eV for molybdenum (Mo 3d) in its highest oxidation state (VI). These values are characteristic of the elements of the Keggin unit ( $\text{PMo}_{12}\text{O}_{40}^{3-}$ ) [50].

XPS spectrum of  $\text{Sn}_{0.5}\text{PMo}_{12}$  (Figure 6c) shows two photo peaks in the range 496–488 eV, characteristic of Sn 3d<sub>5/2</sub> and Sn 3d<sub>3/2</sub>. Based on literature data, the binding energy value of 487.2 eV, does not permit to distinguish between both oxidation states II and IV of tin [26,29]. However, the detection of both Mo(V) 3d<sub>5/2</sub> and Mo(V) 3d<sub>3/2</sub> with binding energies of 232.0 and 235.2 eV, respectively, in addition to those of Mo(VI) 3d<sub>5/2</sub> and Mo(VI) 3d<sub>3/2</sub> with binding

energies of 233.2 and 236.3 eV, respectively [51], indicates that tin may be present also as Sn(IV), results in agreement with those observed in UV-Vis that have evidenced the presence of Mo(V). In conclusion,  $\text{H}_2\text{Sn}_{0.5}\text{PMo}_{12}$  is a compound partially reduced with the presence of both Sn(IV)/Sn(II) and Mo(VI)/Mo(V) couples.

The XPS spectrum of  $\text{Sb}_{0.5}\text{PMo}_{12}$  (figure not shown) displays the presence of three deconvoluted photo peaks with binding energies of 530.9, 532.0 and 533.6 eV revealing the existence of three types of oxygen atoms, that are probably terminal oxygen ( $\text{O}_d$ ), and bridging oxygen atoms ( $\text{O}_b$  and  $\text{O}_c$ ) bonded to molybdenum atoms of the POM framework, as reported by Grinvald *et al.* [52]. On the other hand, the peak associated to Mo 3d was observed with an energy of 233.1 eV (Table 2). The binding energy values of 541.38 and 532.95 eV, given in Table 2 (Figure 6d), can be attributed to Sb 3d<sub>3/2</sub> and Sb 3d<sub>5/2</sub>, respectively, characteristic of oxidation state III, and those of 541.69 and 534.28 eV to Sb 3d<sub>3/2</sub>



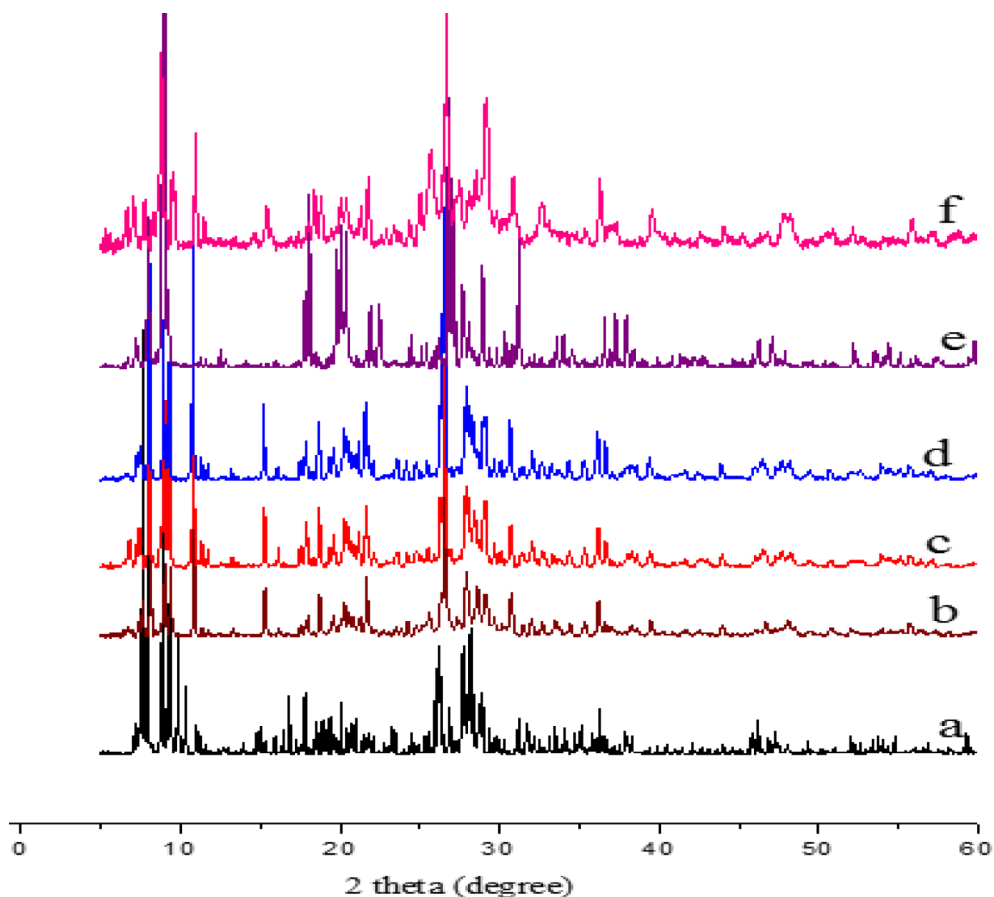


**Figure 4.** XRD patterns of  $\text{H}_3\text{PMo}_{12}\text{O}_{40}$  (a),  $\text{Sn}_{0.25}\text{Sb}_{0.5}\text{PMo}_{12}$  (b),  $\text{Sn}_{0.5}\text{Sb}_{0.5}\text{PMo}_{12}$  (c),  $\text{Sn}_{0.75}\text{Sb}_{0.25}\text{PMo}_{12}$  (d),  $\text{Sb}_1\text{PMo}_{12}\text{O}_{40}$  (e) and  $\text{Sn}_{1.5}\text{PMo}_{12}\text{O}_{40}$  (f).

and Sb  $3d_{5/2}$ , respectively, characteristic of oxidation state V, in accordance with literature data [30,53]. The presence of oxidation state V of antimony confirms, therefore the reduction of Mo(VI) to Mo(V), a result consistent with that observed in the UV-Vis. In conclusion,  $\text{H}_{1.5}\text{Sb}_{0.5}\text{PMo}_{12}$  is also a compound partially reduced with the presence of both Sb(V)/Sb(III) and Mo(VI)/Mo(V).

In the case of mixed salts (Figures 6a and b), the binding energies of the molybdenum atoms at different oxidation degrees of  $\text{Sn}_{0.25}\text{Sb}_{0.25}\text{PMo}_{12}$ , corresponding to the spin states Mo(VI)  $3d_{3/2}$  (233.4 eV), Mo(VI)  $3d_{5/2}$  (236.5 eV), Mo(V)  $3d_{3/2}$  (232.0 eV) and Mo(V)  $3d_{5/2}$  (235.2 eV) and those of  $\text{Sn}_{0.5}\text{Sb}_{0.5}\text{PMo}_{12}$ , Mo(VI)  $3d_{3/2}$  (233.3 eV), Mo(VI)  $3d_{5/2}$  (236.5 eV), Mo(V)  $3d_{3/2}$  (232.0 eV) and Mo(V)  $3d_{5/2}$  (235.2 eV) are similar to those of  $\text{Sn}_{0.5}\text{PMo}_{12}$

Mo(VI)  $3d_{3/2}$  (233.2 eV), Mo(VI)  $3d_{5/2}$  (236.3 eV) Mo(V)  $3d_{3/2}$  (232.0 eV), Mo(V) and  $3d_{5/2}$  (235.2 eV) (figure not shown). The Sn 3d binding energies in  $\text{Sn}_{0.25}\text{Sb}_{0.25}\text{PMo}_{12}$  and  $\text{Sn}_{0.5}\text{Sb}_{0.5}\text{PMo}_{12}$  are of 487.2 and 487.1 eV, respectively, equivalent to those obtained with  $\text{Sn}_{0.5}\text{PMo}_{12}$  (487.5 eV), while the binding energies corresponding to the antimony atoms could not be detected, probably due to its very small amount or due to overlapping with the oxygen peaks.

These results seem to suggest that in the mixed salts, the influence of tin predominates over that of antimony, probably related to the stronger reducing character of tin. The presence of molybdenum in oxidation states (V) and (VI) can only confirm that of Sn(II) and Sn(IV) in the mixed salts.

Table 4 shows the percentage of molybdenum and the Mo(V)/Mo(VI) atomic ratios for  $\text{Sn}_{0.5}\text{PMo}_{12}$ ,

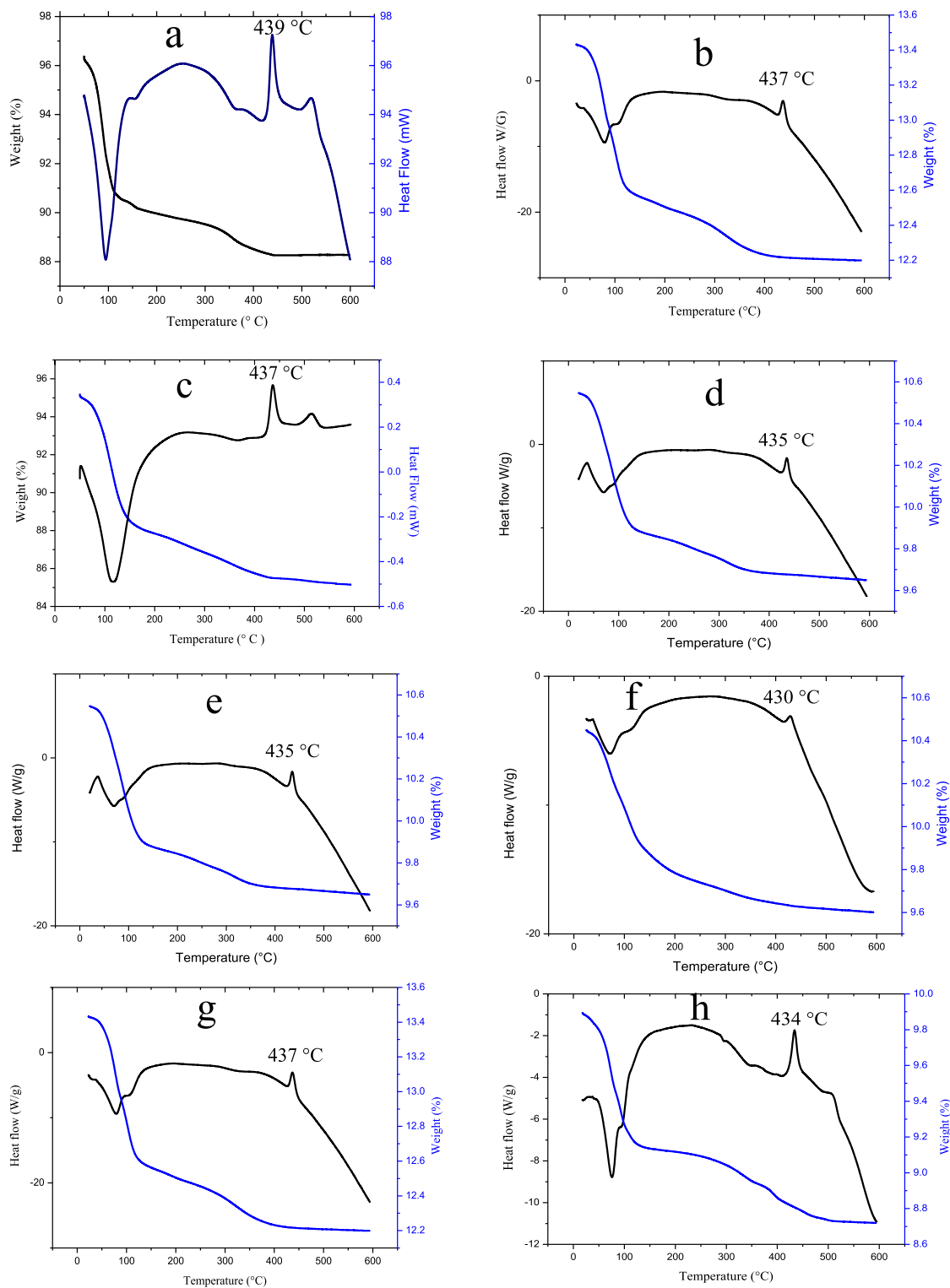


**Figure 5.** TG-DTA diagrams of  $\text{H}_3\text{PMo}_{12}\text{O}_{40}$  (a),  $\text{Sn}_{0.25}\text{Sb}_{0.25}\text{PMo}_{12}$  (b),  $\text{Sb}_1\text{PMo}_{12}$  (c),  $\text{Sn}_{0.25}\text{Sb}_{0.5}\text{PMo}_{12}$  (d),  $\text{Sn}_{0.75}\text{Sb}_{0.25}\text{PMo}_{12}$  (e),  $\text{Sn}_{0.75}\text{Sb}_{0.5}\text{PMo}_{12}$  (f),  $\text{Sn}_{0.5}\text{Sb}_{0.5}\text{PMo}_{12}$  (g) and  $\text{Sn}_{0.25}\text{Sb}_{0.75}\text{PMo}_{12}$  (h).

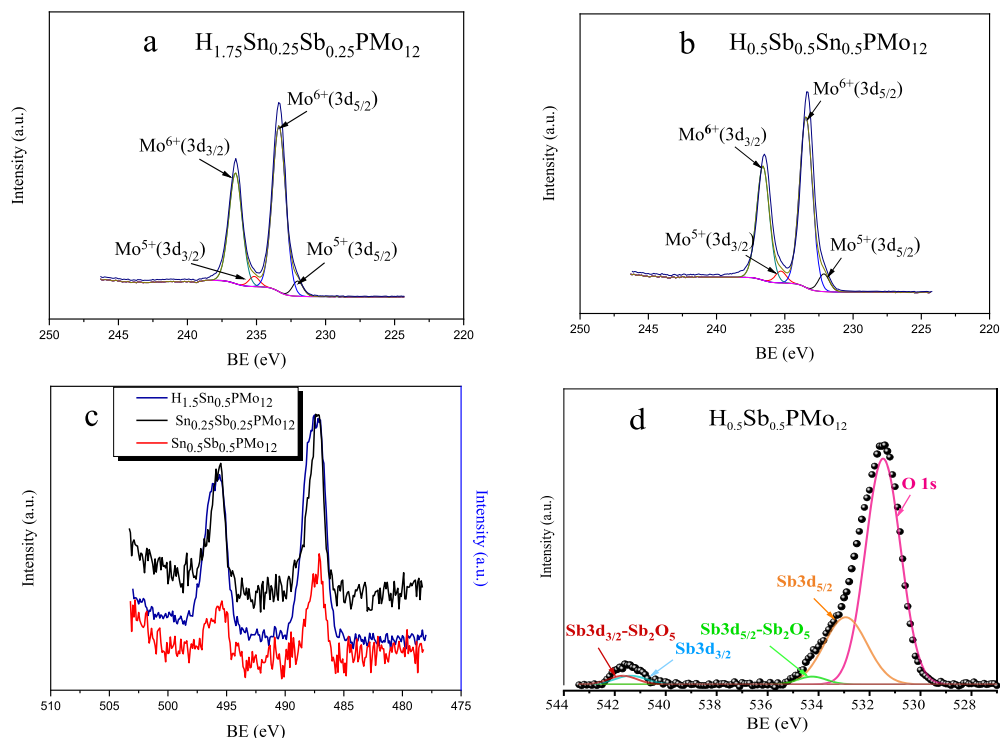


**Figure 6.** XPS spectra of Mo core levels of  $H_{1.75}Sn_{0.25}Sb_{0.25}PMo_{12}O_{40}$  (a),  $H_{0.5}Sn_{0.5}Sb_{0.5}PMo_{12}O_{40}$  (b) and Sn 3d core of:  $H_2Sn_{0.5}PMo_{12}$ ,  $H_{1.75}Sn_{0.25}Sb_{0.25}PMo_{12}O_{40}$ ,  $H_{0.5}Sn_{0.5}Sb_{0.5}PMo_{12}O_{40}$  (c) and Sb 3d + O 1s core of  $H_{0.5}Sb_{0.5}PMo_{12}$  (d).

**Table 2.** Binding energies (eV) of different elements of the heteropolysalts deduced from XPS analysis

	$PMo_{12}$	$Sb_{0.5}PMo_{12}$	$Sn_{0.5}PMo_{12}$	$Sn_{0.25}Sb_{0.25}PMo_{12}$	$Sn_{0.5}Sb_{0.5}PMo_{12}$
O 1s	531.2	531.4	530.9	531.2	531.1
P 2p	134.2	134.4	134.0	134.3	134.4
Mo 3d	233.2	233.1	233.1	233.4	233.3
Mo(VI) $3d_{3/2}$	/		233.2	233.4	233.3
Mo(VI) $3d_{5/2}$	/		236.3	236.5	236.5
Mo(V) $3d_{3/2}$	/		232.0	232.0	232.0
Mo(V) $3d_{5/2}$	/		235.2	235.2	235.2
C 1s	284.8	284.8	284.8	284.8	284.4
Sn 3d	/	/	487.5	487.2	487.1
Sb $3d_{3/2}$ ( $Sb^{3+}$ )	/	541.38			
Sb $3d_{3/2}-Sb_2O_5$ ( $Sb^{5+}$ )	/	541.69			
Sb $3d_{5/2}$	/	532.95			
Sb $3d_{5/2}-Sb_2O_5$	/	534.28			
O 1s	/	530.9			
O 1s	/	532.0			
O 1s	/	533.6			

$\text{Sn}_{0.25}\text{Sb}_{0.25}$  and  $\text{Sn}_{0.5}\text{Sb}_{0.5}$ , determined from the surface percentages calculated in Table 3. For the three salts, the obtained ratios of Mo(VI)/Mo(V) are of 11–13. Referring to the Keggin unit, we can conclude that on average, one Mo atom out of 12 has undergone a reduction.

### 3.1.6. Electrochemical characterization

Figure 7 shows the reversible cyclic voltammograms of aqueous solutions of  $\text{H}_3\text{PMo}_{12}\text{O}_{40}$ ,  $\text{Sn}_{0.5}\text{PMo}_{12}$ ,  $\text{Sb}_{0.5}\text{PMo}_{12}$ ,  $\text{Sn}_{0.25}\text{Sb}_{0.25}\text{PMo}_{12}$  and  $\text{Sn}_{0.5}\text{Sb}_{0.5}\text{PMo}_{12}$ . The valence changes of the Mo species, Mo(VI)/Mo(V), in  $\text{H}_3\text{PMo}_{12}$  exhibits, during cathodic sweep, two peaks at ca. 0.27 and ca.  $-0.13$  V, suggesting two electrochemical reactions with a transfer of two electrons for each step as reported by several authors [54–56]. The tin introduction ( $\text{Sn}_{0.5}\text{PMo}_{12}$ ) leads to a decrease in the reduction potential of molybdenum from 0.27 to 0.15 V, resulting from its pronounced reducing character. This effect was not observed with antimony ( $\text{Sb}_{0.5}\text{PMo}_{12}$ ) and its presence does not seem to influence the oxidizing power of molybdenum. With mixed salts  $\text{Sn}_{0.25}\text{Sb}_{0.25}\text{PMo}_{12}$  and  $\text{Sn}_{0.5}\text{Sb}_{0.5}\text{PMo}_{12}$ , the reduction potential of Mo(VI)/Mo(V) varies slightly (from 0.27 to 0.23 and 0.24 V, respectively). These results are consistent with those observed in UV-Vis and XPS analysis which showed the existence of the redox couples Mo(VI)/Mo(V), Sn(IV)/Sn(II) and Sb(V)/Sb(III).

### 3.2. Catalytic test

Works carried out in our laboratory have shown that a reaction time of 20 h is required to achieve the highest AA yield [17,24,57]. In order to determine the best catalyst/cyclohexanone ratio leading to the highest yield of AA, various preliminary tests were carried out with  $\text{H}_{0.75}\text{Sb}_{0.75}\text{PMo}_{12}\text{O}_{40}$  catalyst, *soluble salt*. The obtained results are represented in Figure 8. An increase in the molar ratio by a factor of 2, from  $1.59 \times 10^{-4}$  to  $3.18 \times 10^{-4}$ , led to a strong increase of AA yield from 26 to 49%. Up to a molar ratio of  $3.18 \times 10^{-4}$ , the AA yield decreases progressively with the increasing molar ratio to reach a value of 33% for a molar ratio of  $9.53 \times 10^{-4}$ . It should be noted that for a ratio of  $2.87 \times 10^{-3}$ , the AA yield is of 42%. So, the molar ratio of  $3.18 \times 10^{-4}$  was fixed for the catalytic tests carried out on all the series of salts.

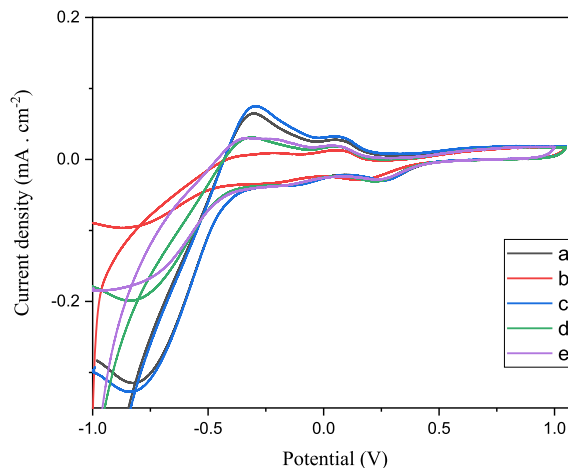


**Figure 7.** Cyclic voltammogram curves of  $\text{H}_3\text{PMo}_{12}\text{O}_{40}$  (a),  $\text{H}_2\text{Sn}_{0.5}\text{PMo}_{12}$  (b),  $\text{H}_{1.5}\text{Sb}_{0.5}\text{PMo}_{12}$  (c),  $\text{H}_{1.75}\text{Sn}_{0.25}\text{Sb}_{0.25}\text{PMo}_{12}\text{O}_{40}$  (d) and  $\text{H}_{0.5}\text{Sn}_{0.5}\text{Sb}_{0.5}\text{PMo}_{12}\text{O}_{40}$  (e) (scan rate:  $10 \text{ mV} \cdot \text{s}^{-1}$ ).

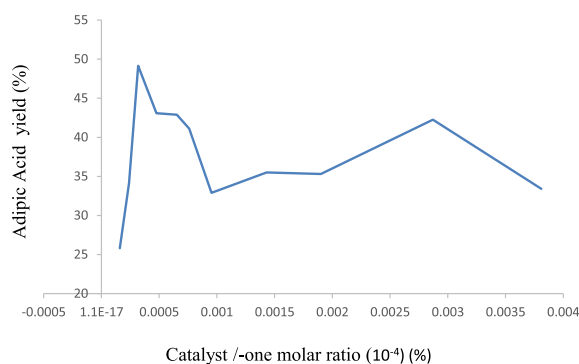


**Figure 8.** AA yield and conversion as function of  $n_{\text{catalyst}}/n_{\text{one molar}}$  ratio, catalyst:  $\text{H}_{0.75}\text{Sb}_{0.75}\text{PMo}_{12}\text{O}_{40}$ . Reaction conditions:  $n_{\text{cyclohexanone}}$ : 90 mmol,  $m_{\text{catalyst}}$ : 0.0625 g, time: 20 h, temperature:  $90^\circ\text{C}$ , mixture agitation rate: 1000 rpm.

Table 5 shows the obtained AA yields over Sn and/or Sb-based salts. In  $\text{H}_x\text{Sb}_y$  series, the highest AA yield was obtained in the presence of salt of formula  $\text{H}_{0.75}\text{Sb}_{0.75}$  with 49 against 44, 24 and 21% for  $\text{H}_0\text{Sb}_1$ ,  $\text{H}_{2.25}\text{Sb}_{0.25}$  and  $\text{H}_{1.5}\text{Sb}_{0.5}$ , respectively. It should be noted that in the absence of proton, the AA yield obtained with  $\text{H}_0\text{Sb}_1$  (44%) is almost twice as high as those obtained with  $\text{H}_{1.5}\text{Sb}_{0.5}$  (21%) and  $\text{H}_{2.25}\text{Sb}_{0.25}$  (24%). These results suggest that the best

**Table 3.** Atomic percentages of different elements of the heteropolysalts deduced from XPS analysis

	PMo <sub>12</sub>	Sb <sub>0.5</sub> PMo <sub>12</sub>	Sn <sub>0.5</sub> PMo <sub>12</sub>	Sn <sub>0.25</sub> Sb <sub>0.25</sub> PMo <sub>12</sub>	Sn <sub>0.5</sub> Sb <sub>0.5</sub> PMo <sub>12</sub>
O 1s	54.2	47.7	53.9	46.1	43.0
P 2p	2.6	1.9	2.4	1.8	1.6
Mo 3d	19.1	14.5	18.0	16.4	14.8
Mo(VI) 3d <sub>3/2</sub>			46.0	46.5	45.8
Mo(VI) 3d <sub>5/2</sub>			46.2	46.6	46.0
Mo(V) 3d <sub>3/2</sub>			3.9	3.4	4.1
Mo(V) 3d <sub>5/2</sub>			3.9	3.5	4.1
C 1s	24.1	36.0	25.2	35.5	40.4
Sn 3d			0.5	0.2	0.1
Sb 3d <sub>3/2</sub> -metal (Sb <sup>3+</sup> )		1.2			
Sb 3d <sub>3/2</sub> -Sb <sub>2</sub> O <sub>5</sub> (Sb <sup>5+</sup> )		0.3			
Sb 3d <sub>5/2</sub> -metal		1.2			
Sb 3d <sub>5/2</sub> -Sb <sub>2</sub> O <sub>5</sub>		0.3			
O 1s		56.8			
O 1s		35.3			
O 1s		4.9			

**Table 4.** Surface atomic ratios of Mo(V)/Mo(VI) and number of Mo(V) and Mo(VI) deduced from XPS analysis

POM	Mo(VI) (at.%)	Mo(V) (at.%)	Mo(V)/Mo(VI)	Mo(VI) number	Mo(V) number
Sn <sub>0.5</sub> PMo <sub>12</sub>	92.2	7.8	0.0846	11.064	0.936
Sn <sub>0.25</sub> Sb <sub>0.25</sub> PMo <sub>12</sub>	93.1	6.9	0.0741	11.172	0.828
Sn <sub>0.5</sub> Sb <sub>0.5</sub> PMo <sub>12</sub>	91.8	8.2	0.0893	11.016	0.984

AA yields were obtained when the Sb atom number is superior to 0.5 per Keggin unit. Among them, H<sub>0.75</sub>Sb<sub>0.75</sub> catalyst was found to be the most efficient.

In H<sub>x</sub>Sn<sub>y</sub> series, the highest AA yield was obtained in the presence of H<sub>1.5</sub>Sn<sub>0.75</sub> with 39 against 28–35% for other salts of the same series. Based on the UV-Vis analysis results and comparing the intensity of the absorption band corresponding to Mo(V), it can be deduced that a moderate reduction state of salt would favor the AA formation.

In the Sn<sub>x</sub>Sb<sub>y</sub> series, the best combination leading to the highest AA yield is H<sub>0.75</sub>Sn<sub>0.75</sub>Sb<sub>0.25</sub> with 37% against 23–35% for the other formulations, similar results to those obtained with the H<sub>x</sub>Sn<sub>y</sub> series. Therefore, the AA production does not seem to be influenced by the Sb addition.

The difference in the catalytic performance between H<sub>0.75</sub>Sb<sub>0.75</sub> and H<sub>1.5</sub>Sn<sub>0.75</sub> can be attributed to the higher oxidation states of the antimony atoms Sb(V)/Sb(III) compared to those of tin Sn(IV)/Sn(II). Thus, a judicious combination of elements in the chemical composition of the salt can lead to an effective catalyst in the cyclohexanone oxidation to AA.

In our previous works [15,17], it was observed by P<sup>31</sup>NMR, after the cyclohexanone oxidation in the presence of hydrogen peroxide, carried out under the same operating conditions as those used in this work, the presence of heteropolyanionic species, different from those observed before oxidation reaction. They were attributed to peroxometallic species. In the case of Sn<sub>1.5</sub>PMo<sub>12</sub>O<sub>40</sub>, SbPMo<sub>12</sub>O<sub>40</sub> and H<sub>3-2x</sub>Sn<sub>x1</sub>Sb<sub>x2</sub>PMo<sub>12</sub>O<sub>40</sub> ( $x = x_1 + x_2$  and  $x = 0-0.75$ ) salts, it can be assumed that the peroxometallic

**Table 5.** Adipic acid yields obtained from cyclohexanone oxidation over Sn- and/or Sb-based salts

$H_xSb_y$	AA yield (%)	$H_xSn_y$	AA yield (%)	$Sn_xSb_y$	AA yield (%)
$H_{2.25}Sb_{0.25}$	24	$H_{2.5}Sn_{0.25}$	30	$H_{0.75}Sb_{0.25}Sn_{0.75}$	37
$H_{1.5}Sb_{0.5}$	21	$H_2Sn_{0.5}$	35	$Sb_{0.5}Sn_{0.25}$	30
$H_{0.75}Sb_{0.75}$	49	$H_{1.5}Sn_{0.75}$	39	$Sb_{0.5}Sn_{0.75}$	26
$H_0Sb_1$	44	$H_1Sn_1$	28	$Sb_{0.25}Sn_{0.25}$	31
		$H_{0.5}Sn_{1.25}$	35	$Sb_{0.5}Sn_{0.5}$	35
		$H_0Sn_{1.5}$	33	$Sb_{0.75}Sn_{0.25}$	23

Reaction conditions:  $n_{catalyst}/n_{one}$  molar ratio =  $3.18 \times 10^{-4}$ , time: 20 h, temperature: 90 °C, mixture agitation rate: 1000 rpm.

species that would constitute the active sites, would be based on molybdenum and also on tin and/or antimony. The peroxometallic species resulting from the Keggin-type HPA decomposition in the presence of hydrogen peroxide have already been reported by several authors [58–60] as  $[W_2O_3(O_2)_4(H_2O)_2]^{2-}$ ,  $[PO_4(WO(O_2)_2)_4]^{3-}$ ,  $[HPO_4(WO(O_2)_2)_2]^{2-}$  and  $[W_2O_3(O_2)_4(H_2O)_2]^{2-}$ ,  $[WO(O_2)_2(H_2O)_2(\mu-O)]^{2-}$ ,  $[W_2O_2(\mu-O_2)(O_2)_2]$ .

#### 4. Conclusion

$Sn_{1.5}PMo_{12}O_{40}$ ,  $SbPMo_{12}O_{40}$  and  $H_{3-2x}Sn_{x1}Sb_{x2}PMo_{12}O_{40}$  ( $x = 2x_1 + 3x_2$  and  $x_1, x_2 = 0-0.75$ ) materials were synthesized, characterized and tested in the cyclohexanone oxidation in the presence of hydrogen peroxide at 90 °C. The cationic exchange method used in the preparation of these salts allowed to fix precisely the stoichiometric coefficients of Sn and Sb atoms.

FT-IR and Raman spectroscopic analysis also showed that the Keggin structure was preserved. UV-Vis and XPS analysis showed that the salts are of mixed valence with oxidation states of Mo(VI)/Mo(V), Sb(V)/Sb(III) and Sn(IV)/Sn(II) and the valence change of the Mo species, Mo(VI)/Mo(V) was confirmed by electrochemical characterization.

The POMs are found to be active in the cyclohexanone oxidation and among them, the most efficient is  $H_{0.75}Sb_{0.75}$  with 49% yield of AA.

#### Conflicts of interest

Authors have no conflict of interest to declare.

#### References

- [1] S. E. Davis, M. S. Ide, R. J. Davis, *Green Chem.*, 2013, **15**, 17-45.
- [2] M. N. Kopylovich, A. P. C. Ribeiro, E. C. B. A. Alegria, N. M. R. Martins, L. M. D. R. S. Martins, A. J. L. Pombeiro, *Adv. Organomet. Chem.*, 2015, **63**, 91-174.
- [3] R. Afrasiabi, M. R. Farsani, B. Yadollahi, *Tetrahedron Lett.*, 2014, **55**, 3923-3925.
- [4] G. Sereda, V. Rajpara, *Green Sustain. Chem.*, 2011, **01**, 26-30.
- [5] M. Aghayi, B. Yadollahi, M. R. Farsani, *J. Iran. Chem. Soc.*, 2020, **17**, 2895-2900.
- [6] W. Jin, P. Zheng, W. T. Wong, G. L. Law, *Adv. Synth. Catal.*, 2017, **359**, 1588-1593.
- [7] X. Deng, H. Cao, C. Chen, H. Zhou, L. Yu, *Sci. Bull.*, 2019, **64**, 1280-1284.
- [8] Y. Song, F. Xin, L. Zhang, Y. Wang, *Chem. Catal. Chem.*, 2017, **9**, 4139-4147.
- [9] J. H. Choi, D. R. Park, S. Park, I. K. Song, *J. Nanosci. Nanotechnol.*, 2011, **11**, 7870-7875.
- [10] N. Mizuno, K. Kamata, K. Yamaguchi, *Top. Catal.*, 2010, **53**, 876-893.
- [11] M. J. da Silva, C. M. De Oliveira, *Curr. Catal.*, 2017, **7**, 26-34.
- [12] N. I. Gumerova, A. Rompel, *Nat. Rev. Chem.*, 2018, **2**, 1-20.
- [13] S. Omwoma, C. T. Gore, Y. Ji, C. Hu, Y. F. Song, *Coord. Chem. Rev.*, 2015, **286**, 17-29.
- [14] A. Patel, N. Narkhede, S. Singh, S. Pathan, *Catal. Rev. - Sci. Eng.*, 2016, **58**, 337-370.
- [15] D. Amitouche, M. Haouas, T. Mazari, S. Mouanni, R. Canioni, C. Rabia, E. Cadot, C. Marchal-Roch, *Appl. Catal. A - Gen.*, 2018, **561**, 104-116.
- [16] J. Alcañiz-Monge, G. Trautwein, A. Garcia-Garcia, *J. Mol. Catal. A - Chem.*, 2014, **394**, 211-216.
- [17] M. Moudjahed, L. Dermeche, S. Benadji, T. Mazari, C. Rabia, *J. Mol. Catal. A - Chem.*, 2016, **414**, 72-77.
- [18] L. Mouheb, L. Dermeche, N. Essayem, C. Rabia, *Catal. Lett.*, 2020, **150**, 3327-3334.
- [19] S. Benadji, T. Mazari, L. Dermeche, N. Salhi, E. Cadot, C. Rabia, *Catal. Lett.*, 2013, **143**, 749-755.
- [20] F. Chami, L. Dermeche, A. Saadi, C. Rabia, *Appl. Petrochem. Res.*, 2013, **3**, 35-45.
- [21] L. Dermèche, C. Rabia, G. Rekhila, M. Trari, *Sol. Energy Mater. Sol. Cells*, 2017, **168**, 45-50.

- [22] M. R. Guerroudj, L. Dermeche, L. Mouheeb, T. Mazari, S. Benadji, C. Rabia, *Bull. Chem. React. Eng. Catal.*, 2019, **14**, 283-293.
- [23] S. Mouanni, D. Amitouche, T. Mazari, C. Rabia, *Appl. Petrochem. Res.*, 2019, **9**, 67-75.
- [24] L. Mouheeb, L. Dermeche, T. Mazari, S. Benadji, N. Essayem, C. Rabia, *Catal. Lett.*, 2018, **148**, 612-620.
- [25] S. Mouanni, T. Mazari, D. Amitouche, S. Benadji, L. Dermeche, C. Roch-Marchal, C. Rabia, *C. R. Chim.*, 2019, **22**, 327-336.
- [26] S. Campisi, C. Evangelisti, G. Postole, A. Gervasini, *Appl. Surf. Sci.*, 2021, **539**, 1-47.
- [27] D. M. Chaves, S. O. Ferreira, R. C. Da Silva, R. Natalino, M. J. Da Silv, *Energy Fuels*, 2019, **33**, 7705-7716.
- [28] M. J. Da Silva, A. A. Julio, S. O. Ferreira, R. C. Da Silva, D. M. Chaves, *Fuel*, 2019, **254**, 1-11.
- [29] A. Lewera, P. J. Barczuk, K. Skorupska, K. Miecznikowski, M. Salamonczyk, P. J. Kulesza, *J. Electroanal. Chem.*, 2011, **662**, 93-99.
- [30] Y. Wang, J. Lu, X. Ma, Y. Niu, V. Singh, P. Ma, C. Zhang, J. Niu, J. Wang, *Mol. Catal.*, 2018, **452**, 67-174.
- [31] G. Xue, X. Liu, H. Xu, H. Hu, F. Fu, J. Wang, *Inorg. Chem.*, 2008, **47**, 2011-2016.
- [32] T. Mazari, S. Benadji, A. Tahar, L. Dermeche, C. Rabia, *J. Mater. Sci. Eng. B*, 2013, **3**, 146-152.
- [33] S. A. Chavan, D. Srinivas, P. Ratnasamy, *J. Catal.*, 2002, **212**, 39-45.
- [34] Y. Deng, L. Ma, Y. Mao, *Biochem. Eng. J.*, 2016, **105**, 16-26.
- [35] S. Van De Vyver, Y. Román-Leshkov, *Catal. Sci. Technol.*, 2013, **3**, 1465-1479.
- [36] Y. Zhou, M. Zhao, S. Zhou, Y. Zhao, G. Li, Y. Deng, *J. Biotechnol.*, 2020, **314-315**, 8-13.
- [37] G. A. Tsigdinos, *Ind. Eng. Chem. Prod. Res. Dev.*, 1974, **13**, 267-274.
- [38] K. Nomiya, M. Miwa, Y. Sugaya, *Polyhedron*, 1984, **3**, 607-610.
- [39] S. X. Xu, X. F. Wu, Q. Y. Wu, W. F. Yan, *Chin. Sci. Bull.*, 2011, **56**, 2679-2682.
- [40] Z. Zhang, B. Wang, Y. Zhang, G. Zhang, Y. Wang, *Adv. Polym. Technol.*, 2019, **2019**, 1-5.
- [41] L. Dermeche, R. Thouvenot, S. Hocine, C. Rabia, *Inorg. Chim. Acta*, 2009, **362**, 3896-3900.
- [42] D. Amitouche, T. Mazari, G. Rekhila, C. Rabia, M. Trari, *J. Inorg. Organomet. Polym. Mater.*, 2019, **30**, 1404-1411.
- [43] S. Ponce, M. Trabold, A. Drochner, J. Albert, B. J. M. Etzold, *Chem. Eng. J.*, 2019, **369**, 443-450.
- [44] I. V. Kozhevnikov, *Chem. Rev.*, 1998, **98**, 171-198.
- [45] M. Sadakane, E. Steckhan, *Chem. Rev.*, 1998, **98**, 219-238.
- [46] N. Mizuno, K. Kamata, *Coord. Chem. Rev.*, 2011, **255**, 2358-2370.
- [47] R. Schlögl, M. Misono, *Chem. Rev.*, 1998, **98**, 199-217.
- [48] M. J. Da Silva, C. B. Vilanculo, M. G. Teixeira, A. A. Julio, *Kinet. Mech. Catal.*, 2017, **122**, 1011-1030.
- [49] D. T. Richens, *The Chemistry of Aqua Ions: Synthesis, Structure and Reactivity: A Tour Through the Periodic Table of the Elements*, Wiley, New York, 1997, 1-567 pages.
- [50] S. Benadji, P. Eloy, A. Léonard, B. L. Su, K. Bachari, C. Rabia, E. M. Gaigneaux, *Micropor. Mesopor. Mater.*, 2010, **130**, 103-114.
- [51] Y. K. Lu, J. N. Xu, X. B. Cui, J. Jin, S. Y. Shi, J. Q. Xu, *Inorg. Chem. Commun.*, 2010, **13**, 46-49.
- [52] E. Grinerval, J. M. Basset, F. Lefebvre, *Inorg. Chim. Acta*, 2011, **370**, 297-303.
- [53] Q. B. Zhang, Y. K. Lu, Y. B. Liu, J. Lu, M. H. Bi, J. H. Yu, T. G. Wang, J. Q. Xu, J. Liu, *Inorg. Chem. Commun.*, 2006, **9**, 544-547.
- [54] S. Wang, Y. Sun, X. Wang, X. Zhang, *Microchim. Acta*, 2005, **149**, 185-191.
- [55] M. Xu, Y. Li, W. Li, C. Sun, L. Wu, *J. Colloid Interface Sci.*, 2007, **315**, 753-760.
- [56] T. Wang, Q. Zhou, X. Ren, Y. Zhou, L. Zhang, F. K. Shehzad, A. Iqbal, *J. Clust. Sci.*, 2019, **30**, 973-984.
- [57] S. Mouanni, T. Mazari, S. Benadji, L. Dermeche, C. Marchal-Roch, C. Rabia, *Bull. Chem. React. Eng. Catal.*, 2018, **13**, 386-392.
- [58] L. Ma, I. Jia, X. Guo, L. Xiang, *Chin. J. Catal.*, 2014, **35**, 108-119.
- [59] S. Zhang, G. Zhao, S. Gao, Z. Xi, J. Xu, *J. Mol. Catal. A - Chem.*, 2008, **289**, 22-27.
- [60] Y. Ding, B. Ma, Q. Gao, G. Li, L. Yan, J. Suo, *J. Mol. Catal.*, 2005, **230**, 121-128.